Journal of Alloys and Compounds 513 (2012) 256–265

Contents lists available at SciVerse ScienceDirect

Journal of Alloys and Compounds

journal homepage: www.elsevier.com/locate/jallcom

Structure and electrical resistivity of $La_{1-x}Ba_xMnO_3$ ($0.25 \leq x \leq 0.35$) perovskites

Irfan Mansuri[a,b], Dinesh Varshney[a,*]

[a] School of Physics, Vigyan Bhavan, Devi Ahilya University, Khandwa Road Campus, Indore 452001, India
[b] Department of Physics, Shri Venkateshwar Institute of Technology, Sanwer Road, Indore 453331, India

ARTICLE INFO

Article history:
Received 28 June 2011
Received in revised form 12 October 2011
Accepted 12 October 2011
Available online 20 October 2011

Keywords:
Oxide materials
Solid state reactions
Crystal structure
X-ray diffraction

ABSTRACT

The structural properties and resistivity of $La_{1-x}Ba_xMnO_3$ ($0.25 \leq x \leq 0.35$) manganites have been investigated. The Rietveld refinement of X-ray powder diffraction patterns fitted using the FullProf refinement program shows that these compounds having a cubic, and hexagonal structure with space group P_{m3m}, and $R\bar{3}c$ for $La_{1-x}Ba_xMnO_3$ ($0.25 \leq x \leq 0.35$). The temperature dependent resistivity curves undergo a metal–semiconductor transition (T_{MS}) at ~200 K ($x = 0.25$), ~220 K ($x = 0.30$) and ~230 K ($x = 0.35$) for $La_{1-x}Ba_xMnO_3$. The temperature dependence of resistivity shows a minimum behavior at low temperatures ($T \leq 50$ K), explained by electron–electron and Kondo-like spin dependent scattering. The metallic resistivity is analyzed, to our knowledge, for the first time highlighting the importance of electron–phonon, electron–electron, and electron–spin fluctuation interactions. For $T > T_{MI}$ the semiconducting nature is discussed with small polaron conduction model.

1. Introduction

Manganites with general formula $RE_{1-x}A_xMnO_3$ (ABO_3 type), where RE is the rare earth element and D is the divalent cation have been studied extensively due to its technological importance viz. colossal magneto-resistance (CMR) and magneto caloric effect along with their rich fundamental physics. The doped manganites exhibit a broad spectrum of magnetic phases like antiferromagnetic insulator, ferromagnetic metallic, and paramagnetic insulator states. The parent $LaMnO_3$ is an antiferromagnetic semiconductor with a magnetic structure of the A type. The Neel temperature for $LaMnO_3$ is approximately 140 K and the presence of Jahn–Teller Mn^{3+} ions with the electronic configuration $t_{2g}^3 e_g^1$ ($S = 2$) enter into stoichiometric $La^{3+}Mn^{3+}O_3{}^{2-}$. Hence, $LaMnO_3$ possess O′-orthorhombic symmetry of unit cell [1–4].

The substitution of a divalent alkaline-earth metal (Ca, Sr, Ba) for a trivalent rare earth at the A site, affects the average ionic radii of the A site and results in the change of the structure of the compound. Usually, $La_{1-x}Ba_xMnO_3$ crystallizes either in cubic or hexagonal lattice structure with space group P_{m3m} and $R\bar{3}c$. Due to the substitution certain percentage of Mn^{3+} is formally replaced with Mn^{4+} enabling charge carriers for electrical conduction. Substitution by alkaline earth elements at the La sites enhances the Mn^{4+} concentration in $LaMnO_3$ effectively. Also, the size of the alkaline earth element affects the Mn^{3+}–O–Mn^{4+} bond angle and the strength of the double exchange ferromagnetic interaction [5]. The ionic radii of the constituent ions are detrimental for the kind as well the degree of distortion of the simple cubic perovskite structure [6].

The Curie temperature (T_C) of doped perovskite $La_{1-x}Ca_xMnO_3$ manganites can be continuously varied by various substitutions [7,8]. Although, the Curie temperature is a non-monotonic function of r_A, reaches a maximum for the composition $La_{2/3}Sr_{1/3}MnO_3$ ($r_A \sim 1.24$ Å). The Ba-doped manganites possess the largest value of ionic radii among the $La_{1-x}A_xMnO_3$ manganites leading to an intrinsically strained structure with crystal lattice parameters close to that of the ideal simple cubic perovskite with the average Mn–O–Mn bond angle increased toward values closer to 180° [9]. It is accepted that the $La_{2/3}Ba_{1/3}MnO_3$ manganite crystallizes in rhombohedral ($R\bar{3}c$) and crystal lattice at room temperature and in orthorhombic lattice of *Imma* space-group symmetry at 1.6 K [10].

Recently, Zainullina and researchers argued that the doping of Yttrium on $La_{0.80}Sr_{0.20}MnO_3$ single crystal reduces the Curie temperature but this reduction can be, however, significantly compensated by the formation of vacancies and also suppresses the structural *Pnma*–$R\bar{3}c$ transition [11]. The study of $Pr_{0.67}Ba_{0.33}MnO_3$ and $Pr_{0.67}Sr_{0.33}MnO_3$ perovskites with considerable difference in their variance σ^2 is reported by Hcini et al. [12]. Both compounds exhibit single orthorhombic *Pnma* crystalline phase and with strongly connected and larger grains for $Pr_{0.67}Sr_{0.33}MnO_3$ than for $Pr_{0.67}Ba_{0.33}MnO_3$ that gives a beginning of single crystal growth in $Pr_{0.67}Sr_{0.33}MnO_3$ case. $Pr_{0.67}Ba_{0.33}MnO_3$ with higher variance exhibits distinct intrinsic (due to grains) and extrinsic (due to grain boundaries) transitions in the resistivity behavior, and with higher transition temperatures [12]. On the other hand

* Corresponding author. Tel.: +91 7312467028; fax: +91 7312526699.
E-mail addresses: vdinesh33@rediffmail.com, vdinesh33@gmail.com (D. Varshney).

0925-8388/$ – see front matter © 2011 Elsevier B.V. All rights reserved.
doi:10.1016/j.jallcom.2011.10.032

the annealing effect on the structural and transport properties of epitaxial $La_{0.7}Ba_{0.3}MnO_3$ thin film is studied and it is argued that Ba doped manganite has an orthorhombic structure with $a = 5.519$ Å, $b = 7.817$ Å, and $c = 5.547$ Å which can also be indexed as a pseudocubic structure with the lattice parameter of $a_0 = 3.912$ Å [13].

For certain values of the electronic doping and of the A-site ionic radius, these compounds are metallic and ferromagnetic at low temperatures, while their conductivity displays semiconducting behavior at high temperatures [3]. The manganites seem to possess a magnetic phase diagram at normal pressure and $La_{0.67}Ba_{0.33}MnO_3$ and $La_{0.7}Ba_{0.3}MnO_3$ displays paramagnetic insulating behavior above T_C; a ferromagnetic metal below this temperature and a magnetoresistance peak in the vicinity of T_C [14–16]. On the other hand, for the ferromagnetic $La_{1-x}Ba_xMnO_3$ ($0.15 \le x \le 0.25$) single crystal manganites have ferromagnetic and paramagnetic states and optical spectra are satisfactorily understood in terms of transitions between energy levels of the MnO_6 complex or between levels of two neighboring Mn ions. Furthermore, for $La_{0.85}Ba_{0.15}MnO_3$ the energy gap is about 0.15–0.20 eV for $T \ll T_C$. However, the gap in the $La_{0.80}Ba_{0.20}MnO_3$ is close to zero, and in the $La_{0.75}Ba_{0.25}MnO_3$ the gap disappears. The $La_{0.75}Ba_{0.25}MnO_3$ undergoes a transition from the metallic state to the semiconductor one somewhat below T_C rather than at $T = T_C$ [17].

On the theoretical side at low temperatures, the contribution from the electron–lattice interaction is weakened and the Coulomb correlation effects are substantial. Henceforth, the low-temperature transport properties of the doped manganites may reflect the intrinsic mechanism of the systems. Beside the distinct low-field magnetoresistance at low temperatures, experimental reports provide evidence for the existence of the resistivity minimum at low temperatures in the manganites, no matter the polycrystalline, the quality film, or the single crystal, which is similar to the Kondo effect [18,19]. On the other hand, for the strongly correlated system, there may be another contribution arising from the renormalization of the effective electron–electron interactions, which can modify the density of the states at the Fermi energy and enhanced the resistivity [20,21]. Earlier we noticed in the theoretical study of $La_{1-x}Na_xMnO_3$ ($x = 0.1, 0.17$) manganites, that the electron–phonon, electron–electron and electron–magnon scattering must be an important cause of resistivity in the metallic state while small polaron conduction is responsible for conductivity behavior in insulating (or semiconducting) state [22].

With these motivations, we have prepared Ba^{2+} doped ($25\% \le x \le 35\%$) $La_{1-x}Ba_xMnO_3$ manganites by solid-state route technique to seek the role of substitution effects (divalent cation Ba^{2+} for trivalent La^{3+}) on the structural and magnetic properties following X-ray diffraction (XRD), energy dispersive X-ray analysis (EDAX), scanning electron microscopy (SEM), and *dc* electrical resistivity.

The main findings for $La_{1-x}Ba_xMnO_3$ ($0.25 \le x \le 0.35$) manganites include:

(i) the structure of these manganites is cubic and hexagonal phase with P_{m3m}, and $R\bar{3}c$ space group settings,
(ii) the unit-cell volume and also tolerance factor t increased with increases the doping concentration of Ba in La manganites,
(iii) the EDAX results confirm purity and chemical composition of these compounds,
(iv) the SEM results reveal that compositions are homogeneous and the particle sizes are in the range of 3–5 μm,
(v) the temperature dependent resistivity undergo a metal–semiconductor transition (T_{MS}) at ~200 K ($x = 0.25$), ~220 K ($x = 0.30$) and ~230 K ($x = 0.35$) for $La_{1-x}Ba_xMnO_3$,
(vi) the magnitude of resistivity is suppresses when applying the magnetic field, shows the existence of CMR effect,
(vii) at low temperatures ($T \le 50$ K), a resistivity upturn is observed along with a $T^{1/2}$ dependence of the resistivity is due to electron–electron interactions (Coulomb interaction), and $\ln T$ contribution due to Kondo-like spin dependent scattering,
(viii) the metallic region of these manganites in the temperature range ($50 \le T \le T_{MS}$) is retraced by using spin-fluctuation mechanism ($T^{4.5}$ dependence of the resistivity), electron–electron contribution with T^2 dependence of the resistivity and electron–phonon interaction (T^5 dependence of the resistivity),
and
(ix) the small polaron conduction (SPC) model consistently explains the higher temperature resistivity behavior ($T > T_{MS}$).

2. Experimental details

2.1. Synthesis

We synthesized a series of Ba doped Lanthanum manganites having the general formula, $La_{1-x}Ba_xMnO_3$ ($0.25 \le x \le 0.35$) by conventional solid-state reaction method. Mixture of stoichiometric amount of La_2O_3, $BaCO_3$, and MnO_2 was calcined (at 900 °C) in air for 24 h with two intermediate grindings and then sintered (at 1000 °C) for 24 h after being palletized. The pellets were finally annealed at 1000 °C in oxygen atmosphere [23].

2.2. Characterization

2.2.1. X-ray diffraction (XRD)

The X-ray diffraction (XRD) measurements were carried out with Cu Kα radiation using a Rigaku powder diffractometer equipped with a rotating anode scanning (0.01° step in 2θ) over the angular range 10–90° at room temperature generating X-ray by 40 kV and 100 mA power settings. Monochromatic X-rays of $\lambda = 1.5406$ Å $K_{\alpha 1}$ line from a Cu target were made to fall on the prepared samples. The diffraction pattern was obtained by varying the scattering angle 2θ from 10° to 90° in step size of 0.01°. XRD data were refined by means of the Rietveld method using the FullProf refinement program [24].

2.2.2. Scanning electron microscopy (SEM) and energy-dispersive X-ray analysis (EDAX)

High-resolution scanning electron microscopy (SEM) and energy-dispersive X-ray analysis (EDAX) have been done using an INSA Oxford instrument model no. JEOL - JSM 5600 with 3.5 nm resolution, 18–300,000× (in 136 steps) magnification and 0.5–30 kV (53 steps) accelerating voltage.

2.2.3. Iodometric titration

The ratio of the Mn^{3+}/Mn^{4+} concentration and oxygen content of the samples was determined by iodometric titration. Typically, about 100 mg of the sample was dissolved in 10 ml of 1:10 HCl containing about 1 g of solid KI. Liberated iodine was titrated against standard sodium thiosulphate (0.04 N) solution using starch as an indicator.

2.2.4. dc electrical resistivity

Electrical resistivity measurements were carried out by standard four-probe method in the temperature range 5–300 K. Electrical contacts were made using Indium on a rectangular rod of the sample. We have used a Stanford Research Systems lock-in amplifier (model SR 850) and commercial Lakeshore controllers (model DCR93CA).

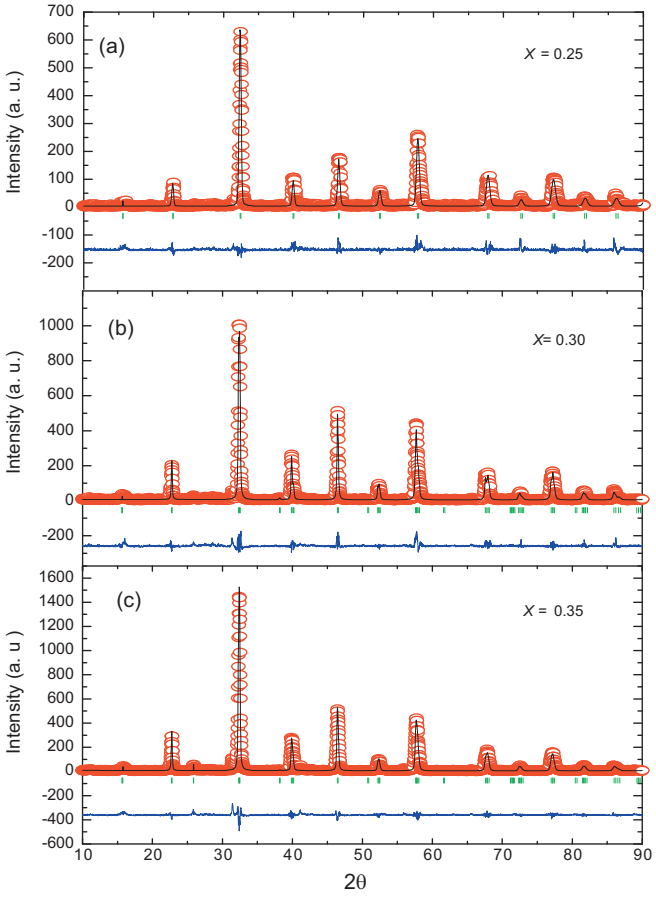

Fig. 1. The X-ray diffraction patterns of the compounds $La_{1-x}Ba_xMnO_3$ ($0.25 \le x \le 0.35$) with Rietveld refinements (a–c, respectively), circles indicate the experimental data and the calculated data is the solid black lines overlapping them. The lowest curve shows the difference between experimental and calculated patterns. The vertical bars indicate the expected reflection positions.

3. Results and discussion

At room temperature the Rietveld refinement XRD patterns show that the $La_{1-x}Ba_xMnO_3$ samples is cubic ($x = 0.25$) and hexagonal ($x = 0.30$ and 0.35) lattice structure with space group P_{m3m} ($x = 0.25$) and $R\bar{3}c$ ($x = 0.30$ and 0.35) for $La_{1-x}Ba_xMnO_3$, respectively as illustrated in Fig. 1 and is consistent with previous results [10]. Back ground Rietveld refinements [24] were fitted with a polynomial function; a pseudo-Voigt function was employed to model the peak shape and two asymmetry parameters were used. All reflections could be indexed and a good level of agreement between the observed and calculated XRD patterns for these samples was obtained. The structural parameters are listed in Table 1 along with the values of the residual factor R_p and the weighted residual factor R_{wp}.

It is noticed that the lattice parameters increases with enhanced Ba substitution at the A-site, and also the unit-cell volume shows a progressive expansion. As Ba^{2+} is substituted for La^{3+} enhances the concentration of Mn^{3+} in the structure, which is larger than Mn^{4+}. Although the effective ionic radius of Ba^{2+} (1.34 Å) is larger than that of La^{3+} (1.061 Å) and considering stoichiometric phases, so an expansion of the cell volume was comprehensible. One of possible origins of the lattice distortion of perovskite-based structures is the deformation of the $Mn^{3+}O_6$ octahedra originating from the JT effect that is inherent to the high-spin ($S = 2$) Mn^{3+} ions with double degeneracy of the e_g orbital. Obviously, this kind of distortion is directly related to the concentration of Mn^{3+} ions.

Table 1
Structure data from X-ray powder diffraction studies of $La_{1-x}Ba_xMnO_3$ ($0.25 \le x \le 0.35$). The atoms are located at the following Wyckoff positions for P_{m3m} ($x = 0.25$) and $R\bar{3}c$ ($x = 0.30$ and 0.35) space group (cubic and hexagonal setting, respectively), La/Ba, 1(a): (0, 0, 0); Mn 1(b): (1/2, 1/2, 1/2); O 1(c): (1/2, 1/2, 1/2); La/Ba, 6(a): (0, 0, 1/4); Mn 6(b): (0, 0, 0); O 18(e): (*X*, 0, 1/4) and La/Ba, 6(a): (0, 0, 1/4); Mn 6(b): (0, 0, 0); O 18(e): (*X*, 0, 1/4). The bond lengths correspond to each unit cell. R_p, and R_{wp}, are the residual factor, and the weighted residual factor.

Composition			
x	0.25	0.30	0.35
Lattice parameters			
a (Å)	3.9091	5.5361	5.5379
c (Å)	–	13.4744	13.4888
V (Å^3)	59.7352	412.9688	413.6791
Bond distances			
La/Ba–O (Å)	2.7256	2.7618	2.7633
Mn–O (Å)	1.9601	1.9609	1.9611
Positional parameter of Oxygen			
O(1)–O(2) (Å)	1.6900	2.762	3.1070
Tolerance factor			
t	0.875	0.880	0.885
Residual factors			
R_p	0.356	0.265	0.245
R_{wp}	0.43	0.351	0.344
χ^2	1.98	1.96	2.12
Ratio of manganese ions (using iodometric titration)			
Mn^{4+} (%)	26.38	31.57	36.75
Mn^{3+} (%)	73.61	68.42	63.24
Mn^{4+}/Mn^{3+} (%)	35.84	46.14	58.11
Oxygen content			
δ (in $MnO_{3+\delta}$)	0.00691	0.00785	0.00878

On the other hand the tolerance factor $t = (r_A + r_O)/\sqrt{2}\,(r_B + r_O)$ (where r_A, r_B, and r_O, are the ionic radii for A-site, Mn-site and Oxygen ion, respectively), which is a quantitative measure of the structural perfection of the ABO_3 perovskites, was calculated by using the average values for r_A and r_B and are presented in the Table 1. It is noticed that when we increase the amount of Ba^{2+} ion doping at La^{3+} site, the Mn–O–Mn bond angle and the tolerance factor is also increased, because the ionic radii of Ba^{2+} ion is larger then that of La^{3+} ion. Based on the structural results of Ba-doping systems, it is inferred that the structure symmetry of doped perovskite manganese oxides is affected by the size of doped ions.

The stoichiometry of the $La_{1-x}Ba_xMnO_3$ ($0.25 \le x \le 0.35$) samples is confirmed by energy dispersive X-ray analysis (EDAX) as shown in Fig. 2. The atomic percentages are listed in Table 2. We have observed that the prepared samples have no impurity and the precursors have fully undergone the chemical reaction to form the expected perovskite material. The reason for EDAX characterization was to ratify the purity and surety of the chemical composition. Scanning electron micrographs of all the samples are also shown in the inset of Fig. 2. The micrograph of samples shows voluminous and porous morphology and the particle sizes are in the range of 3–5 μm consistent with earlier observations $La_{0.95}Na_{0.045}MnO_{3.075}$ manganites [25]. Shivakumara and researchers argued that the scanning electron micrographs of as-synthesized $La_{0.95}Na_{0.045}MnO_{3.075}$ manganites prepared by the solution combustion method shows voluminous and porous morphology and the calcination results in the growth of particle size

Table 2
EDAX results for $La_{1-x}Ba_xMnO_3$ ($0.25 \le x \le 0.35$) manganites.

Element present	Atomic percentages		
	$x = 0.25$	$x = 0.30$	$x = 0.35$
La	12.35	12.14	11.82
Ba	3.15	4.17	5.85
Mn	13.95	14.27	15.60
O	70.55	69.42	66.73

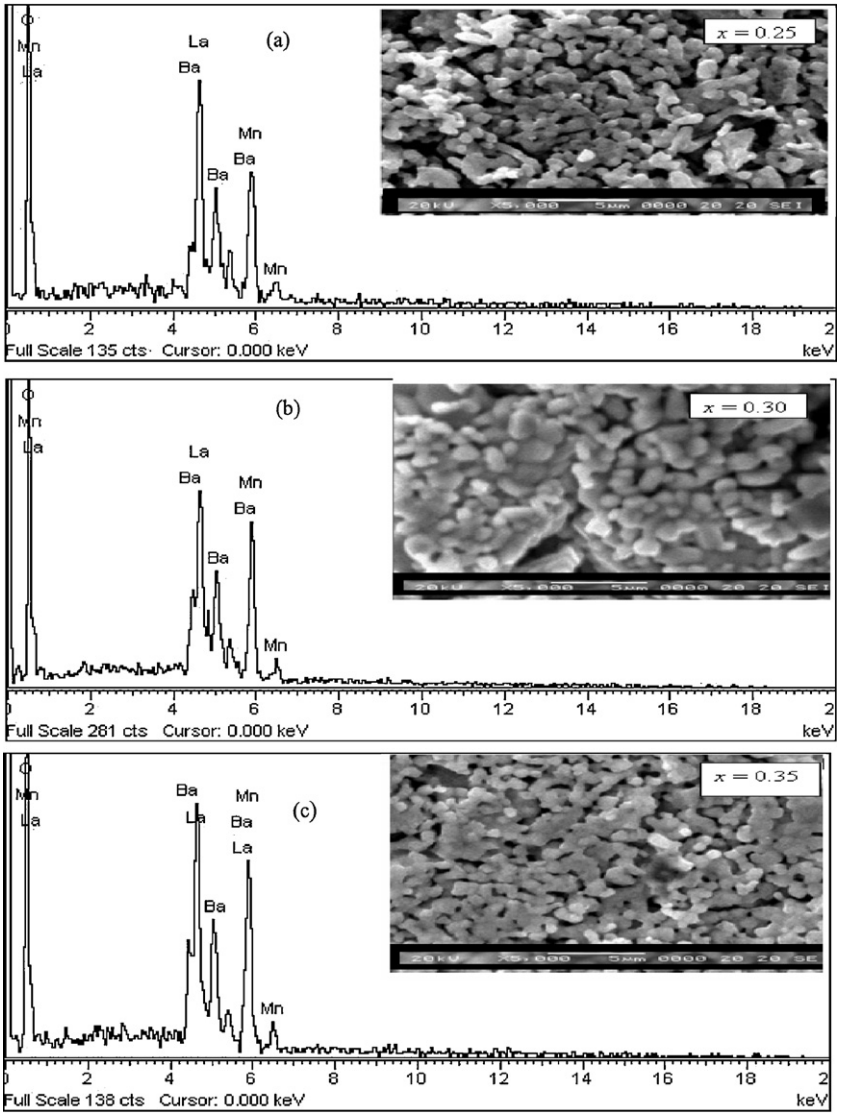

Fig. 2. The EDAX spectrum of $La_{1-x}Ba_xMnO_3$ ($0.25 \le x \le 0.35$) compounds and the insets are the Scanning electron micrographs (a–c, respectively).

and grain boundary and agglomeration of the particles. It is worth to mention microstructures developed during synthesis process influences the structural and electrical properties. The effect of the pores and grain size on the transport and structural properties of manganites has not been focused in the present studies and shall studied in future.

The scanning electron microscopy (SEM) results reveal that compositions are homogeneous. Also, because the samples were prepared by solid-state reaction method, there may be oxygen deficiency which cannot be ruled out. Therefore, before measurement, the samples were annealed in oxygen at 1000 °C for 12 h.

If it is assumed that, La and Ba are present in all the samples in there respective stoichiometric ratio and Mn is present in a mixed valence state ($Mn^{3+}$and Mn^{4+}), then the chemical formula of the compounds can be written as: $La_{1-x}{}^{3+}Ba_x{}^{2+}Mn_{1-\Delta}{}^{3+}Mn_{\Delta}{}^{4+}O_{3+\delta}$ ($0.25 \le x \le 0.35$), where $\delta = (\Delta - x)/2$. The value of Δ (and hence the values of the Mn^{3+} and Mn^{4+} contents) is determined by iodometric titration method [26]. Typically, about 100 mg of the sample was dissolved in 10 ml of 1:10 HCl containing about 1 g of solid KI. The following reactions occur:

$$2Mn^{3+} + 2Cl^- \rightarrow Cl_2 + 2Mn^{2+}$$

$$Mn^{4+} + 2Cl^- \rightarrow Cl_2 + Mn^{2+}$$

$$Cl_2 + 2I^- \rightarrow 2Cl^- + I_2$$

Liberated iodine was titrated against standard sodium thiosulphate (0.04 N) solution using starch as an indicator. The value of Δ (and hence the values of the Mn^{3+} and Mn^{4+} contents) can be determined by using the volume V of sodium thiosulphate solution used in titration as:

$$\Delta = \frac{(M - 16x)NV - m}{m - 8NV}$$

where m is the mass, M is the molecular weight of the sample and N is the normality of the standard sodium thiosulphate solution. The calculated values of the Mn^{4+}/Mn^{3+} ratio and oxygen content (δ) of the samples are illustrated in Table 1. It is noticed that if we increased the doping concentration of Ba^{2+} ions at La^{3+} site in $La_{1-x}Ba_xMnO_3$ manganites the percentage of Mn^{4+} is increased and Mn^{3+} is decreased. As a result the ratio of Mn^{4+}/Mn^{3+} also increases with increased doping concentration. It is also observed that the oxygen content is sufficient in all the samples.

The temperature dependence of the resistivity at 0 and 8 T magnetic fields for $La_{1-x}Ba_xMnO_3$ ($0.25 \le x \le 0.35$) between 5 and

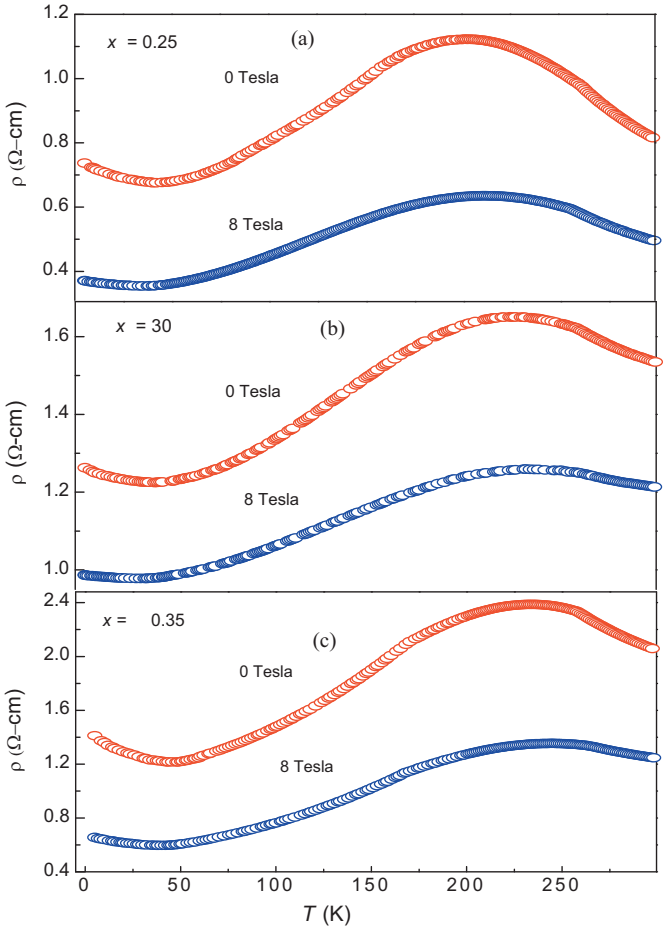

Fig. 3. The temperature dependence of the resistivity without and with 8 T of magnetic field for $La_{1-x}Ba_xMnO_3$ ($0.25 \le x \le 0.35$) between 5 and 300 K (a–c, respectively).

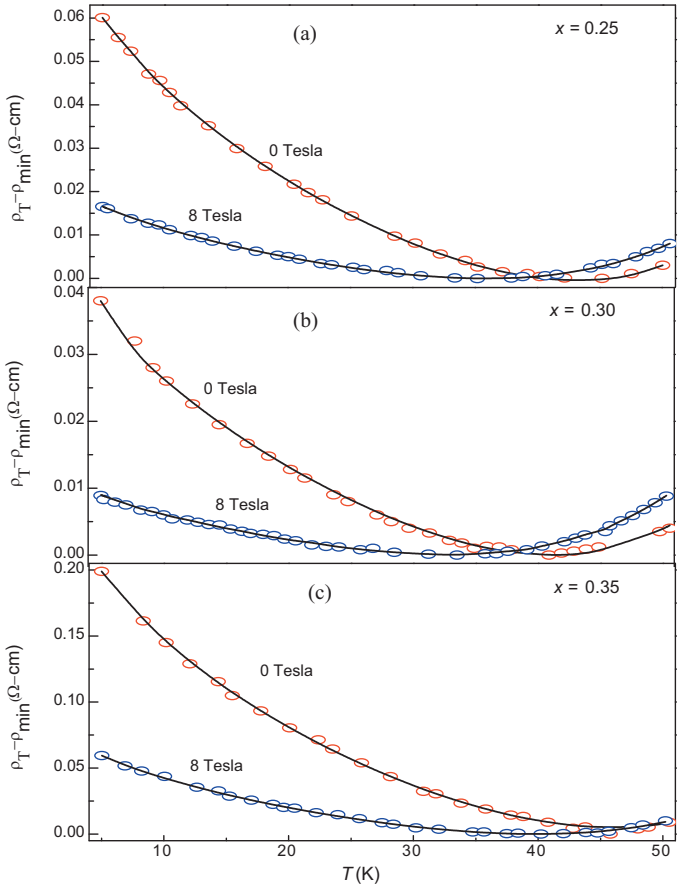

Fig. 4. Temperature dependence of the resistivity for $La_{1-x}Ba_xMnO_3$ ($0.25 \le x \le 0.35$) samples in the ferromagnetic region at low temperatures. The solid lines are the best fit to Eq. (1) (a–c, respectively).

300 K is depicted in Fig. 3(a)–(c). The temperature dependent resistivity behavior is suppressed in the temperature range of 5–300 K on an application of 8 T fields, which infers the existence of the CMR effect. All the samples exhibit metallic behavior at below metal-semiconductor transition temperature (T_{MS}) and semiconductor-like features above T_{MS}. The value of T_{MS} increases from ~200 K, ~220 K and ~230 K as the Ba content increases from 0.25 to 0.35. The magnitude of the resistivity in the entire temperature range increases with increasing Ba concentration in the samples. It may be noted that in the case of Ba doping, for every amount of x of Ba^{2+}, an amount of Mn^{3+} will get converted to Mn^{4+}. As a result, even a small amount of Ba doping results in a large number of charge carriers in the e_g band and results in decrease in the resistivity. However, at low temperatures (~50 K), the resistivity of all the samples shows upturn on lowering the temperature consistent with the earlier reports [19,27–30].

The temperature dependence of resistivity and the change of corresponding characteristic parameters under various applied fields between 0 and 8 T in the temperature range of 5–50 K for the $La_{1-x}Ba_xMnO_3$ ($0.25 \le x \le 0.35$) samples shown in Fig. 4(a)–(c). In order to understand the origin of the observed resistivity minimum in manganites, the experimental data had been analyzed taking account of Kondo-like scattering, the electron–electron interaction, weak localization, intergranular tunneling of the polarized charge carriers, and so on [19,27–30]. Tiwari and coworkers [29] explain the low-temperature electrical resistivity minimum observed in $La_{0.7}A_{0.3}MnO_3$ (A = Ca, Sr, Ba) perovskite oxides in terms of a $T^{1/2}$ dependence of conductivity, which is a characteristic of 3D disordered metallic systems with enhanced electron–electron interactions due to disorder. The origin of such unusual contribution has been attributed to Coulomb interaction (CI) between carriers strongly enhanced by disorder inherent in manganites. It is argued that along with the electron–electron interactions, Kondo-like spin dependent scattering should also contribute to the resistivity minimum for polycrystalline $La_{2/3}Ca_{1/3}MnO_3$ sample for lower fields ($H < 1.0$ T) [27].

The resistivity minimum at low temperatures should be due to the competition of scattering mechanisms. It is noticed that one, usually, increases and the other, decreases with the increase in the temperature. The contribution of the electron–phonon interaction to the resistivity increases with the enhanced temperature. While to that, the contributions from the electron–electron and the spin-disorder scattering decrease with the enhanced temperature.

We have thus fitted the low-temperature ($T < 50$ K) resistivity data to the expression

$$\rho(T) = \frac{1}{\sigma_0 + \sigma_e\sqrt{T}} - C\ln T + \rho_p(T)^5 \quad (1)$$

Herein, the first term σ_0, the residual conductivity contributed by the temperature-independent scattering processes and σ_e represents the contribution of electron–electron scattering to the resistivity. The second term reflects the Kondo-like spin dependent scattering and the third term corresponds to the electron–phonon interaction.

The $\rho(T)$ data for all the samples without magnetic field at low temperatures are fitted to Eq. (1) shown in Fig. 4. The $\rho(T)$ behavior in the absence of magnetic field is retraced by incorporating both

Table 3
Parameters obtained corresponding to the best fit to the experimental data of $La_{1-x}Ba_xMnO_3$ samples below 50 K at 0 and 8 T magnetic fields.

x	σ_0 (Ω^{-1} cm^{-1})	σ_e (Ω^{-1} cm^{-1} K$^{-1/2}$)	$\rho_p \times 10^{11}$ (Ω cm K^{-5})	$C \times 10^3$ (Ω cm K^{-1})
No magnetic field				
0.25	1.28	0.03	5.80	0.40
0.30	0.78	0.02	6.12	0.20
0.35	0.64	0.02	6.49	0.20
Magnetic field of 8 T				
0.25	2.61	0.04	5.00	–
0.30	1.97	0.03	5.33	–
0.35	1.43	0.03	5.57	–

electron–electron interactions (Coulomb interaction) in terms of $T^{-1/2}$ dependence and the Kondo-like spin dependent scattering in terms of ln T dependence consistent with the previous arguments [27]. At higher fields $H = 8$ T, the $\rho(T)$ is successfully fitted with a $T^{1/2}$ dependence of conductivity (please see Fig. 4). Herein, the Kondo-like spin dependent scattering, with $C \ln T$ from Eq. (1) is not taken in to account again consistent with the previous arguments [27]. The parameters corresponding to the best fit for both $H = 0$ and 8 T are given in Table 3.

It should be noticeable that the residual conductivity σ_0 decreases with the increase of doping concentration and field, which is different from the usual conductors. Usually in good conductors, σ_0 should not depend on temperature and magnetic field H. In fact, this may be related to the intrinsic properties of the system and does reflect CMR effect and disorder characteristics for the manganites. As far as the electron–phonon (ρ_p) interaction is concerned, it is insensitive to the applied fields, because it is smaller than the other coefficients by several orders and this interaction is increased when we increased the doping concentration and decreased on the application of magnetic field. It is noticeable the electron–electron contribution and Kondo-like spin dependent scattering contribution has been suggested that the resistivity minimum at low temperatures come from the competition of two contributions: one, usually, increases and the other decreases with the increase of the doping concentration. As shown in Table 3, we have fitted the resistivity behavior at 8 T field without accounting of Kondo-like spin dependent scattering.

With a view to understand the conduction mechanism of divalent Ba doped $La_{1-x}Ba_xMnO_3$ manganites, in metallic region ($T < T_{MS}$), we take into account fluctuation-induced thermal broadening effects, the another possibility of high-energy optical phonons like acoustic and optical phonons in order to estimate the temperature-dependent resistivity, and another possibility for the change in carrier density arises due to the presence of electron–electron correlation in the metallic system. Therefore, we try to fit the metallic resistivity data to the expression [31]

$$\rho(T) = \rho_0 + \rho_{sf}(T) + \rho_{e-e}(T) + \rho_{e-ph}(T) \tag{2}$$

Here, the first term is the residual resistivity, second term is spin fluctuation mechanism and other two terms on the right-hand side of Eq. (2) are related to the electron–electron contribution and electron–phonon contribution.

The second term is

$$\rho_{sf}(T) = \rho_{res}\left[\frac{1}{4} + \frac{1}{\pi}\tan^{-1}\left(\frac{T - T_{sf}}{T_{sf}}\right)\right] \tag{3}$$

where ρ_{res} and T_{sf} is the residual contribution of resistivity and spin fluctuation temperature is given by

$$T_{sf} = \frac{\hbar T_C \pi^2}{6 - x} \tag{4}$$

Here, T_C is the critical temperature and x is the doping concentration. The third term is

$$\rho_{e-e}(T) = BT^2 \tag{5}$$

with

$$B = \frac{k_B^2}{\hbar\omega_P^2 \varepsilon_0 E_F} \tag{6}$$

Here, ω_p is the plasmon frequency, $\varepsilon_0 = 8.85 \times 10^{-12}$ F/m is the vacuum permittivity and E_F is the Fermi energy.

The last term of Eq. (2) is due to the electron–phonon contribution which is explained by the Bloch–Gruneisen (BG) method to estimate the independent contributions of acoustic and optical phonons. The temperature dependent part of the resistivity, following the Debye model [32]:

$$\rho(T) \approx \left(\frac{3}{\hbar e^2 v_F^2}\right)\frac{k_B T}{M v_s^2}\int_0^{2k_F} |F(q)|^2 \left[\frac{x q^3 dq}{[e^x - 1][1 - e^{-x}]}\right] \tag{7}$$

with $x = \hbar\omega/k_B T$. In the above, $F(q)$ is the Fourier transform of the potential associated with one lattice site, v_F being the Fermi velocity. v_s being the sound velocity. Eq. (7) in terms of acoustic phonon contribution yields the Bloch–Gruneisen function of temperature dependence resistivity:

$$\rho_{ac}(T, \theta_D) = 4A_{ac}T\left(\frac{T}{\theta_D}\right)^4 \int_0^{\theta_D/T} x^5 (e^x - 1)^{-1}(1 - e^{-x})^{-1} dx \tag{8}$$

where A_{ac} is a constant of proportionality defined as

$$A_{ac} \cong \frac{3\pi^2 e^2 k_B}{k_F^2 v_s^2 L \hbar v_F^2 M} \tag{9}$$

On the other hand, in case of the Einstein type of phonon spectrum (an optical mode) $\rho_{op}(T)$ may be described as follows:

$$\rho_{op}(T, \theta_E) = A_{op}{\theta_E}^2 T^{-1}[e^{\theta_E/T} - 1]^{-1}[1 - e^{-\theta_E/T}]^{-1} \tag{10}$$

A_{op} is defined analogously to Eq. (9). Thus, the phonon resistivity can be conveniently modeled by combining both terms arising from acoustic and optical phonons

$$\rho_{e-ph}(T) = \rho_{ac}(T, \theta_D) + \rho_{op}(T, \theta_E) \tag{11}$$

For the temperature dependent resistivity analysis one needs the value of Debye (Einstein) temperature and has been estimated using an effective interionic interaction potential (EIoIP) with the long-range Coulomb, van der Waals (vdW) interaction and the short-range repulsive interaction up to second neighbor ions within the Hafemeister and Flygare approach. The essentials are illustrated in Appendix A and the computed values of materials parameter required for the estimation of Debye (Einstein) temperatures using the structural parameters and Bulk modulus are documented in Table 4.

Fig. 5(a)–(c) illustrates the results of temperature dependence of resistivity data points and the theoretical fit in the metallic region following the spin fluctuation, electron–electron, and electron phonon contribution following Eq. (6). The coefficient of spin

Table 4
The material dependent parameters (b, ρ) and the second order elastic constants for $La_{1-x}Ba_xMnO_3$ ($0.25 \le x \le 0.35$) manganites.

x	Model parameters				Second order elastic constants		
	b_1 (La/Ba–O) (10^{-12} erg)	ρ_1 (La/Ba–O) (Å)	b_2 (Mn–O) (10^{-12} erg)	ρ_2 (Mn–O) (Å)	$C_{11} \times 10^{-12}$ (Dyne cm^{-2})	$C_{12} \times 10^{-12}$ (Dyne cm^{-2})	$C_{44} \times 10^{-12}$ (Dyne cm^{-2})
0.25	1.248	0.322	4.537	0.359	11.74	8.243	5.179
0.30	1.362	0.317	5.029	0.354	8.016	4.895	3.644
0.35	1.290	0.315	4.461	0.366	7.463	4.317	3.136

Table 5
The estimated parameters at metallic region for $La_{1-x}Ba_xMnO_3$ ($0.25 \le x \le 0.35$) manganites.

x	T_C (K)	ρ_{res} (Ω cm)	T_{sf} (K)	$B \times 10^5$ (Ω cm K^{-2})	ω_p (meV)	E_F (meV)	θ_D (K)	θ_E (K)	$A_{ac} \times 10^7$ (Ω cm K^{-1})	$A_{op} \times 10^7$ (Ω cm K^{-1})
At 0 T field										
0.25	245	0.64	420	1.39	4.78	171	488	608	1.3	1.2
0.30	340	1.18	589	1.15	4.99	189	423	567	1.5	1.4
0.35	352	1.32	615	1.06	5.17	191	405	540	1.7	1.5
At 8 T field										
0.25	245	0.34	420	0.86	6.18	165	488	608	0.5	0.3
0.30	340	0.66	589	0.69	6.85	168	423	567	0.6	0.4
0.35	352	0.85	615	0.61	7.23	169	405	540	0.8	0.5

fluctuation term (Curie temperature, spin fluctuation temperature), electron–electron term (plasmon frequency, Fermi energy) and electron–phonon term (optical and acoustic proportionality constant, Debye temperature, and Einstein temperature) is listed in Table 5.

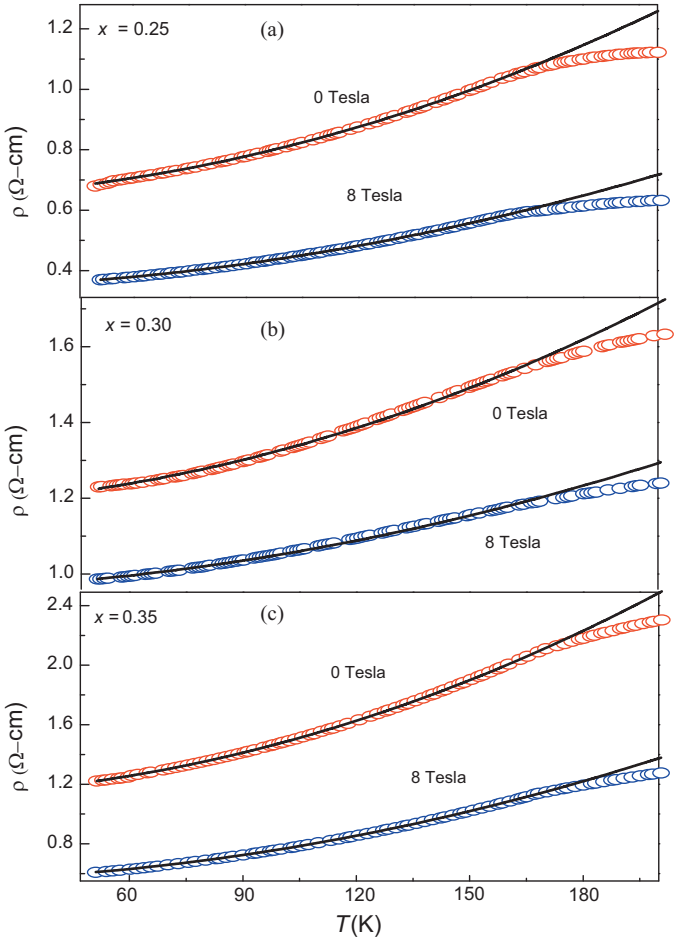

Fig. 5. Temperature dependence of the resistivity for $La_{1-x}Ba_xMnO_3$ ($0.25 \le x \le 0.35$) samples in the metallic region. The solid lines are the best fit to Eq. (2) (a–c, respectively).

The reported behavior of electrical resistivity in doped manganites is analyzed in the framework of the additional model of electron–phonon interaction using the model phonon spectrum consisting of two parts: an acoustic branch of Debye type and optical mode with characteristic Einstein temperature. For the sake of simplicity, a single (longitudinal and transverse) optical phonon mode has been considered, with a flat dispersion relation. The high-energy optical phonon yields a large contribution to the resistivity and is attributed to significant optical phonon hardening effect on carrier transport.

It is noticed from the plot that the computed metallic resistivity leads to a consistent fit the observed behavior incorporating electron–electron and spin fluctuation contribution apart from electron–phonon contribution. The plasmon frequency (Fermi energy) shows an increasing trend on raising the Ba doping and is attributed to enhanced electron–electron interaction. It is noteworthy to comment that in conventional metals, the electron–electron contribution to the resistivity can at best be seen only at low temperatures, due to its small magnitude in comparison with the phonon contribution. The existence of quadratic temperature dependence of resistivity over a wide temperature interval permits one to believe that the electron–electron scattering is also significant in determining the resistivity in manganites.

The observation of power temperature dependence of resistivity indeed points toward electron–electron scattering. The extra contribution arising from the electron–electron contribution is required in manganites to analyze the resistivity behavior. Hence, it is appropriate to use the Bloch–Gruneisen expression in estimating the electron–phonon contributions. The electron scattering rate at low temperature is inversely proportional to Fermi energy and the value of ε_F is low in doped manganites as compared to conventional metals, which implies that the low value of ε_F enhances the electron–electron scattering rate at low temperatures. Thus, along with electron–phonon contribution, the spin fluctuations and electron–electron contributions are essential leading to a qualitative and quantitative agreement between the calculated and measured values. Although, we have provided a simple explanation of these effects, there is a clear need for good theoretical understanding of the resistivity behavior, in view of the fact that formation of small polarons may be of magnetic origin in manganites.

We have further analyzed the resistivity data of high temperature region, $T > T_{MS}$, using adiabatic small polaron conduction (SPC) model. Above the metal–semiconductor transition temperature (T_{MS}), the Jahn–Teller-type distortion present in the unit cell traps

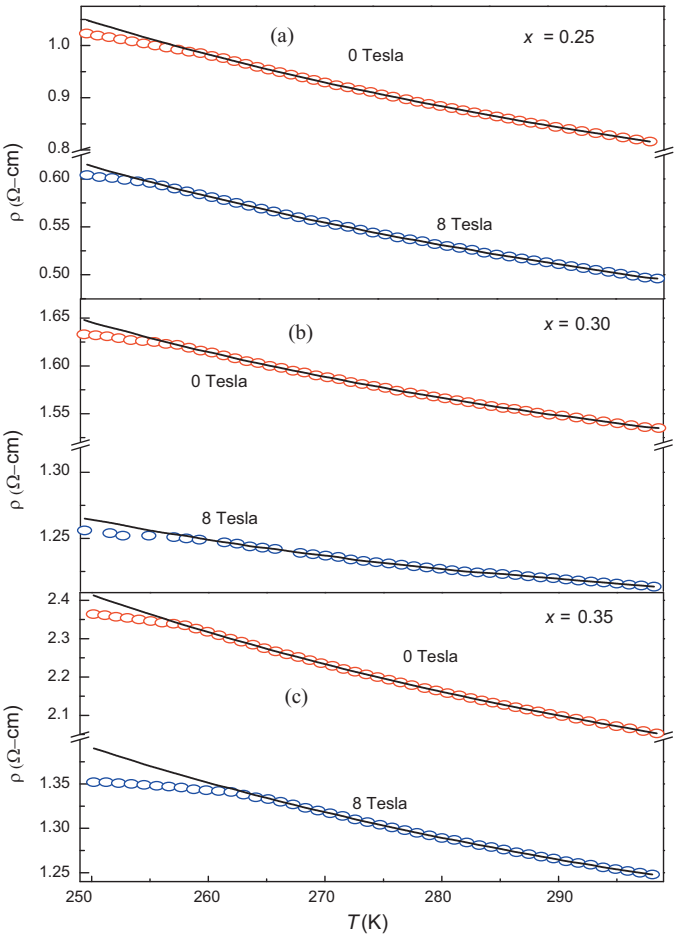

Fig. 6. Variation of semiconducting resistivity with temperature for $La_{1-x}Ba_xMnO_3$ ($0.25 \le x \le 0.35$) (a–c, respectively). The solid line is the fit to $\rho = \rho_p T \exp(E_P/k_B T)$.

the charge carriers and gives rise to polarons. We must mention that the most rapid motion of a small polaron occurs when the carrier hops each time the configuration of vibrating atoms in an adjacent site coincides with that in the occupied site. Henceforth, the charge carrier motion within the adiabatic regime is faster than the lattice vibrations and the resistivity for SPC follows $\rho = \rho_p T \exp(E_P/k_B T)$ with the polaron formation energy E_p and Boltzman constant k_B [23,33].

In the above expression $\rho_p = k_B/n(1-x)e^2D$, where n is the charge carrier density, x is the doping fraction, e is the electronic charge, and D is the polaron diffusion constant ($D = a^2\nu/6$ for a typical cubic coordination where a is being the lattice constant and ν, the characteristic frequency of the longitudinal optical phonon that carries the polaron through the lattice). The fitted curves are shown by thick solid lines in Fig. 6 and the fitting parameters are illustrated in Table 6. It is noticed that if we raised the doping of divalent Ba at La site in manganites the polaron formation energy is increased and charge carrier density is decreased as the disorderness is increased and the contribution of Mn^{4+} ion is also increased, which confirms that the observed resistivity is due to the systematic increase of charge carriers with divalent substitution.

Table 6
Parameters obtained corresponding to the best fit to the experimental data of $La_{1-x}Ba_xMnO_3$ samples by using SPC model.

x	$n \times 10^{-21}$ (cm^{-3})	$B \times 10^4$ (Ω cm K^{-1})	E_P (meV)
At 0 T field			
0.25	3.4	3.697	78
0.30	3.6	3.439	69
0.35	3.9	3.182	64
At 8 T field			
0.25	4.2	2.912	75
0.30	4.5	2.712	63
0.35	4.9	2.681	59

4. Conclusions

Conclusively, the structural and the electrical resistivity of the polycrystalline $La_{1-x}Ba_xMnO_3$ ($0.25 \le x \le 0.35$) are investigated. The structure of these compounds is cubic and hexagonal phase with P_{m3m}, and $R\bar{3}c$ space group settings. The unit-cell volume as well the tolerance factor t increases on increasing the doping amount of Ba at La sites. The EDAX results suggest that the samples are fully undergone the chemical reaction to form the expected perovskite material, and also confirms purity and chemical composition. The micrograph of samples shows voluminous and porous morphology and the particle sizes are in the range of 3–5 μm and compositions are homogeneous.

The electrical resistivity of all the samples shows metal–semiconductor transition at transition temperature T_{MS}, and the magnitude of resistivity is suppressed under the application of magnetic to trace the existence of CMR effect. At low temperatures (below 50 K) in the ferromagnetic region, along with metallic conductivity, a resistivity upturn is observed and retraced with a $T^{1/2}$ is Coulomb type contribution, and Kondo-like spin dependent scattering with $\ln T$ dependence of the resistivity.

The metallic behavior of resistivity for $La_{1-x}Ba_xMnO_3$ manganites in the temperature range ($50 \le T \le T_{MS}$) is retraced by using spin-fluctuation mechanism, electron–electron contribution and electron–phonon interaction. In the high temperature region, $T > T_{MS}$, the resistivity data is analyzed using adiabatic small polaron conduction model. The E_p gradually increases with doping and is due to phonon softening effect on carrier transport owing to Jahn–Teller distortions in the $La_{1-x}Ba_xMnO_3$. We must admit that La–Ba–MnO_3 is less explored. The metallic resistivity is analyzed, to our knowledge, for the first time highlighting the importance of electron–phonon, electron–electron, and electron–spin fluctuation interactions. For $T > T_{MI}$ the semiconducting nature is discussed with small polaron conduction model.

Acknowledgements

Authors are thankful to UGC-DAE CSR, Indore for providing characterization facilities. We acknowledge Dr. R. Rawat, Dr. R.J. Choudhary, Dr. D.M. Phase, and Mr. V. Ahire for their support in carrying out measurements.

Appendix A. Appendix A

The understanding of the dynamical properties of materials requires the formulation of an effective interionic potential and is of substantial importance, as there is much disagreement as to whether long- or short-range interactions are at the origin of the properties of doped manganites. While developing a specific model, we assume that the change in force constants is small; the short-range interactions are effective up to the second-neighbor ions; and the atoms are on hold by elastic forces in the harmonic approximation without any internal strains within the crystal. The crystal energy for a particular lattice separation (r) as:

$$U(r) = U_C(r) + U_R(r) + U_V(r). \quad \text{(A-1)}$$

The first term is the Coulomb energy, and follows:

$$U_C(r) = -\sum_{ij} \frac{Z_i Z_j e^2}{r_{ij}} = -\frac{\alpha_m Z^2 e^2}{r}, \tag{A-2}$$

with α_m as the Madelung constant [34] and r_{ij} being the separation distance between i and j ions.The short-range overlap repulsive energy is the second term in Eq. (A-1) as:

$$U_R(r) = nb\beta_{ij}\ \exp\left(\frac{r_i + r_j + r_{ij}}{\rho}\right) + n'b\beta_{ii}\ \exp\left(\frac{2r_i - kr_{ij}}{\rho}\right) + n'b\beta_{jj}\ \exp\left(\frac{2r_j - kr_{ij}}{\rho}\right) \tag{A-3}$$

following Hafemeister and Flygare [35]. The notations r_i (r_j) refers to the ionic radii, k is the structure factor, $n(n')$ is the number of nearest (next nearest) ions, respectively. Further, the notations b and ρ denote the hardness and range parameters, respectively.

The Pauling coefficients, β_{ij} are defined in terms of valence [Z_i (Z_j)] and number of the outermost electrons [n_i (n_j)] in the anions (cations), respectively as:

$$\beta_{ij} = 1 + \left(\frac{Z_i}{n_i}\right) + \left(\frac{Z_j}{n_j}\right). \tag{A-4}$$

The last term in Eq. (A-1) is the van der Waals (vdW) energy, denoted as:

$$U_v(r) = -\left(\sum_{ij} \frac{c_{ij}}{r_{ij}^6} + \sum_{ij} \frac{d_{ij}}{r_{ij}^8}\right) \tag{A-4a}$$

$$U_v(r) = -\left(\frac{C}{r^+} + \frac{D}{r^8}\right), \tag{A-4b}$$

due to dipole–dipole (d–d) and dipole–quadruple (d–q) interactions. The abbreviations C and D represent the overall vdW coefficients, defined as [34]:

$$C = c_{ij}S_6(r) + \frac{1}{2}(c_{ii} + c_{jj})S_6(0), \tag{A-5a}$$

and

$$D = d_{ij}S_8(r) + \frac{1}{2}(d_{ii} + d_{jj})S_8(0) \tag{A-5b}$$

c_{ij} and d_{ij} are the vdW coefficients due to d–d and d–q interactions. We follow the variational method [36] to derive c_{ij} and d_{ij} as:

$$c_{ij} = \frac{3}{2}\frac{e\hbar}{\sqrt{m_e}}\alpha_i\alpha_j\left[\left(\frac{\alpha_i}{N_i}\right)^{1/2} + \left(\frac{\alpha_j}{N_j}\right)^{1/2}\right]^{-1}, \tag{A-6a}$$

and

$$d_{ij} = \frac{27}{8}\frac{\hbar^2}{m}\alpha_i\alpha_j\left[\left(\frac{\alpha_i}{N_i}\right)^{1/2} + \left(\frac{\alpha_j}{N_j}\right)^{1/2}\right]^2 \left[\left(\frac{\alpha_i}{N_i}\right) + \frac{20}{3}\left(\frac{\alpha_i\alpha_j}{N_iN_j}\right)^{1/2} + \left(\frac{\alpha_j}{N_j}\right)\right]^{-1}. \tag{A-6b}$$

Here, m_e is the electron mass, α_i is the electronic polarisability and N_i denotes the effective number of electrons of the ith ion. The values of the overall vdW coefficients are obtained using Eqs. (A-5) and (A-6), and weighted in terms of appropriate lattice sums [$S_6(0)$, $S_6(r)$, $S_8(0)$ and $S_8(r)$] [34]. We believe that there is no uncertainty involved in the evaluation of c_{ij} and d_{ij}, due to the fact that the excitation energies are ignored in Eqs. (A-6a) and (A-6b). While applying for manganites herein, the above description, we shall seek the interionic interaction in between a pair such as Mn–O and La/Ba–O.

It is clear from the above descriptions that the present effective interionic potential contains only two free parameters (b and ρ), which are determined from the equilibrium conditions:

$$\left(\frac{dU}{dr}\right)_{r=r_0} = 0, \tag{A-7a}$$

and Bulk modulus

$$B_T = \frac{1}{9kr_0}\left(\frac{d^2U}{dr^2}\right)_{r=r_0}. \tag{A-7b}$$

While estimating these values, we use the Bulk modulus from experiment [37] and r_0 (obtained from Rietveld refinement of XRD data). The model parameters obtained from Eqs. (A-7a) and (A-7b) have been used to compute the second order elastic constants (C_{11}, C_{12} and C_{44}) as [38]

$$C_{11} = \frac{e^2}{4r_0^4}\left[-5.112Z_m^2 + A_1 + \frac{A_2 + B_2}{2}\right], \tag{A-8a}$$

$$C_{12} = \frac{e^2}{4r_0^4}\left[-0.226Z_m^2 + B_1 + \frac{A_2 + 5B_2}{2}\right], \tag{A-8b}$$

$$C_{44} = \frac{e^2}{4r_0^4}\left[2.556Z_m^2 + B_1 + \frac{A_2 + 3B_2}{4}\right], \tag{A1-8c}$$

where (A_1, B_1) and (A_2, B_2) are the short-range parameters for the nearest and the next nearest neighbors, respectively. These parameters are further defined as

$$A_1 = \frac{4r_0^3}{e^2}\left[\frac{d^2}{dr^2}V_{ij}(r)\right]_{r=r_0}, \tag{A-9a}$$

$$A_2 = \frac{4(r_0\sqrt{2})^3}{e^2}\left[\frac{d^2}{dr^2}V_{ii}(r) + \frac{d^2}{dr^2}V_{jj}(r)\right]_{r=r_0\sqrt{2}}, \tag{A-9b}$$

$$B_1 = \frac{4r_0^3}{e^2}\left[\frac{d}{dr}V_{ij}(r)\right]_{r=r_0}, \tag{A-10a}$$

$$B_2 = \frac{4(r_0\sqrt{2})^2}{e^2}\left[\frac{d}{dr}V_{ii}(r) + \frac{d}{dr}V_{jj}(r)\right]_{r=r_0\sqrt{2}}, \tag{A-10b}$$

where $V_{ij}(r)$ is the short-range potentials between the ions, which follow

$$V_{ij}(r) = b\beta_{ij}\ \exp\left(\frac{r_i + r_j + r_{ij}}{\rho}\right) + c_{ij}r_{ij}^{-6} + d_{ij}r_{ij}^{-8}. \tag{A-11}$$

Deduced values of the second order elastic constants are illustrated in Table 4. The elastic force constant κ is derived at the equilibrium inter-ionic distance r_0 following

$$\kappa = \frac{r_0}{2}\left[\pi^2(C_{11} - C_{12})(C_{11} + C_{12} + 2C_{44})(C_{44})\right]^{1/3}. \tag{A-12}$$

We have thus estimated the elastic force constants for a pair such as Mn–O and La/Ba–O and have the total force constants of the Ba doped $LaMnO_3$. This continuum model thus takes care of the clear physical binding in doped manganites incorporating van der Waals interactions. However, the true potential must recognize the correct charge distribution and the relative orientations of the interacting atoms in manganites which is a complicated task.

We shall now estimate the acoustic Debye branch characterized by the Debye temperature θ_D and an optical peak defined by the Einstein temperature θ_E. The Debye frequency is characterized as a cut off frequency at the Brillouin zone boundary. It can be expressed in terms of effective value of ionic mass and elastic force constant for crystal lattices with two different kinds of atoms such as Mn–O

and La/Ba–O, which we deal with. The acoustic-mode and optical-mode frequencies are estimated in an ionic model using a value of effective ion charge $Ze = -2e$.

We choose an acoustic mass $M = (2M_+ + M_-)$ [Mn(O) which is symbolized by $M_+(M_-)$], $\kappa^* = 2\kappa$ for each directional oscillation mode to get the acoustic phonon frequency as [39,40]

$$\omega_D - \sqrt{\frac{2\kappa^*}{M}}. \tag{A-13}$$

Furthermore, when the phonons belong to optic modes, their frequency is determined by the reduced mass as $\mu^{-1} = M(\mathrm{A})^{-1} + M(\mathrm{B})^{-1}$ where A is the anion (La/Ba, Mn) and B is the cation (O)

$$\omega_{LO}^2 = \frac{\kappa + \eta}{\mu}, \tag{A-14}$$

$$\omega_{TO}^2 = \frac{\kappa - \eta}{\mu}, \tag{A-15}$$

where η is the force constant as

$$\eta = \frac{8\pi}{3}\frac{(Ze)^2}{\Omega}, \tag{A-16}$$

ω_{LO} (ω_{TO}) symbolized for the longitudinal (transverse) optical phonon frequency and Ω for the volume of the unit cell. We must mention that these computed values for $La_{1-x}Ba_xMnO_3$ with $0.25 \geq x \geq 0.35$ could not be compared due to the lack of the experimental data. However, the computed values of Debye and Einstein temperature for $La_{0.67}Ba_{0.33}MnO_3$ are consistent with the previous specific heat (Raman) measurements [41,42].

It is true that the two-orbital model based on Wannier functions predicts the electronic states such as charge ordering in manganites. As mentioned the Wannier function approach of the electronic problem is useful for the description of electron dynamics following semi-classical theory as well as the magnetic interactions in solids [40]. In the present investigations, we do not intended to discuss the electron dynamics as well the magnetic interactions, but focused on determining the acoustic (optical) phonon frequency to estimate the electron–phonon contribution of resistivity in the ferromagnetic metallic phase.

Earlier, Millis [43] determines the elastic parameters using a mean field approximation with emphasis on Mn–O bond lengths to evaluate the Mn–Mn and Mn–O force constants for the lattice distortions. However, we have considered both Mn–O and La/Ba–O bond lengths to obtain the Mn–O, La/Ba–O force constant and total force constants for strong electron–phonon interaction. The formulated effective interionic interaction potential includes the long-range Coulomb, van der Waals (vdW) interaction and the short-range repulsive interaction up to second neighbor ions within the Hafemeister and Flygare approach. The interionic interaction in between a pair such as Mn–O and La/Ba–O enable us to find the total force constant with consistent Debye and Einstein temperatures.

The developed effective interionic interaction potential thus takes care of the interactions in between a pair such as Mn–O and La/Ba–O. The interactions thus are attractive Coulomb, and van der Waals (vdW) as well as short-range overlap repulsive interaction following Hafemeister and Flygare type potential. The advantage of using this potential is that it takes care of number of nearest (next nearest) ions, the valence, and number of the outermost electrons in the anions (cations), respectively. Thus it takes care of the structural parameters that yield an approximately correct description of the interactions between a pair such as Mn–O and La/Ba–O. Henceforth; we are able to estimate the acoustic and optical phonon frequency consistent with the Specific heat and Raman measurements to estimate the electron–phonon contribution of resistivity.

References

[1] M.B. Salamon, M. Jaime, Rev. Mod. Phys. 73 (2001) 583.
[2] V. Moshnyaga, K. Samwer, Ann. Phys. 523 (2011) 652–663.
[3] Y. Tokura, N. Nagosa, Science 288 (2000) 468.
[4] G. Matsumoto, J. Phys. Soc. Jpn. 29 (1970) 606.
[5] J. Fontcuberta, B. Martinez, A. Seffar, S. Pinol, J.L. Garcia-Munoz, X. Obradors, Phys. Rev. Lett. 76 (1996) 1122.
[6] P. Schiffer, A.P. Ramirez, W. Bao, S.W. Cheong, Phys. Rev. Lett. 75 (1995) 3336.
[7] Y. Samancıoğlu, A. Coşkun, J. Alloys Compd. 507 (2010) 380.
[8] M.H. Phan, V. Franco, N.S. Bingham, H. Srikanth, N.H. Hur, S.C. Yu, J. Alloys Compd. 508 (2010) 238.
[9] W. Archibald, J.S. Zhou, J.B. Goodenough, Phys. Rev. B 53 (1996) 14445.
[10] N. Moutis, I. Panagiotopoulos, M. Pissas, D. Niarchos, Phys. Rev. B 59 (1999) 1129.
[11] R.I. Zainullina, N.G. Bebenin, V.V. Ustinov, Ya.M. Mukovskii, J. Alloys Compd. 467 (2009) 22.
[12] S. Hcini, S. Zemni, A. Triki, H. Rahmouni, M. Boudard, J. Alloys Compd. 509 (2011) 1394.
[13] B. Li, L. Yang, J. Tian, X. Wang, H. Zhu, T. Endo, J. Appl. Phys. 109 (2011) 073922.
[14] P.G. Radaelli, G. Iannone, M. Marezio, H.Y. Hwang, S.W. Cheong, J.D. Jorgensen, D.N. Argyriou, Phys. Rev. B 56 (1997) 8265.
[15] S.N. Barilo, G.L. Bychkov, L.A. Kurnevich, S.V. Shiryaev, L.A. Kurochkin, J.W. Lynn, L. Vasiliu-Doloc, J. Cryst. Growth 211 (2000) 480.
[16] P. Zhang, T.L. Phan, S.C. Yu, J. Supercond. Nov. Magn. (2011), doi:10.1007/s10948-011-1252-z.
[17] N.G. Bebenin, N.N. Loshkareva, A.A. Makhnev, E.V. Mostovshchikova, L.V. Nomerovannaya, E.A. Gan'shina, A.N. Vinogradov, Y.M. Mukovskii, J. Phys.: Condens. Matter 22 (2010) 096003.
[18] I.O. Troyanchuk, D.D. Khalyavin, S.V. Trukhanov, H. Szymczak, J. Phys.: Condens. Matter 11 (1999) 8707.
[19] E. Syskakis, G. Choudalakis, C. Papastaikoudis, J. Phys.: Condens. Matter 15 (2003) 7735.
[20] M. Ziese, Phys. Rev. B 68 (2003) 132411.
[21] J. Kondo, Prog. Theor. Phys. 32 (1964) 37;
P.A. Lee, T.V. Ramakrishnan, Rev. Mod. Phys. 57 (1985) 287.
[22] D. Varshney, D. Choudhary, M.W. Shaikh, E. Khan, Eur. Phys. J. B 76 (2010) 327.
[23] D. Varshney, I. Mansuri, N. Kaurav, J. Phys. Condens. Matter 19 (2007) 246211;
D. Varshney, I. Mansuri, J. Low Temp. Phys. 162 (2011) 52;
I. Mansuri, D. Varshney, N. Kaurav, C.L. Lu, Y.K. Kuo, J. Magn. Magn. Mater. 323 (2011) 316.
[24] J. Rodriguez-Carvajal, FULLPROF version 3.0.0, Laboratorie Leon Brillioun, CEA–CNRS, 1995.
[25] C. Shivakumara, M.B. Bellakki, A.S. Prakash, N.Y. Vasanthacharya, J. Am. Ceram. Soc. 90 (2007) 3852.
[26] J. Spooren, R.I. Walton, J. Franck Millange, Mater. Chem. 15 (2005) 1542.
[27] Y. Xu, J. Zhang, G. Cao, C. Jing, S. Cao, Phys. Rev. B 73 (2006) 224410.
[28] D. Kumar, J. Sankar, J. Narayan, R.K. Singh, A.K. Majumdar, Phys. Rev. B 65 (2002) 094407.
[29] A. Tiwari, K.P. Rajeev, Solid State Commun. 111 (1999) 33.
[30] M. Auslender, A.E. Kar'kin, E. Rozenberg, G. Gorodetsky, J. Appl. Phys. 89 (2001) 6639.
[31] S. Sergeenkov, A.J.C. Lanfredi, F.M. Araujo-Moreira, JETP Lett. 85 (2007) 592.
[32] D. Varshney, M.W. Shaikh, I. Mansuri, J. Alloys Compd. 486 (2009) 726.
[33] A.S. Alexandrov, N.F. Mott, Polarons and Bipolarons, World Scientific, Singapore, 1995.
[34] M.P. Tosi, Solid State Phys. 16 (1964) 1.
[35] D.W. Hafemeister, W.H. Flygare, J. Chem. Phys. 43 (1965) 795.
[36] J.C. Slater, J.G. Kirkwood, Phys. Rev. 37 (1931) 682.
[37] V. Markovich, I. Fita, R. Puzniak, E. Rozenberg, C. Martin, A. Wisniewski, A. Maignan, B. Raveau, Y. Yuzhelevskii, G. Gorodetsky, Phys. Rev. B 70 (2004) 024403.
[38] D. Varshney, U. Sharma, N. Kaurav, J. Phys. Condens. Matter 20 (2008) 075204.
[39] D. Varshney, N. Kaurav, Eur. Phys. J. B 40 (2004) 129.
[40] N. Marzari, D. Vanderbilti, Phys. Rev. B 56 (1997) 12847.
[41] J.M.D. Coey, M. Viret, L. Ranno, K. Ounadjela, Phys. Rev. Lett. 75 (1995) 3910.
[42] J.J. Hamilton, E.L. Keatley, H.L. Ju, A.K. Raychaudhuri, V.N. Smolyaninova, R.L. Greene, Phys. Rev. B 54 (1996) 14926.
[43] A.J. Millis, Phys. Rev. B 53 (1996) 8434.